Turbocharger Radial Turbine Response to Pulse Amplitude

Roberto Mosca[1]
KTH Royal Institute of Technology,
CCGEx,
Department of Engineering Mechanics,
Stockholm 10044, Sweden
e-mail: rmosca@mech.kth.se

Shyang Maw Lim
KTH Royal Institute of Technology,
CCGEx,
Department of Engineering Mechanics,
Stockholm 10044, Sweden
e-mail: smlim@mech.kth.se

Mihai Mihaescu
KTH Royal Institute of Technology,
CCGEx,
Department of Engineering Mechanics,
Stockholm 10044, Sweden
e-mail: mihai@mech.kth.se

Under on-engine operating conditions, a turbocharger turbine is subject to a pulsating flow and, consequently, experiences deviations from the performance measured in gas-stand flow conditions. Furthermore, due to the high exhaust gases temperatures, heat transfer further deteriorates the turbine performance. The complex interaction of the aerothermodynamic mechanisms occurring inside the hot-side, and consequently the turbine behavior, is largely affected by the shape of the pulse, which can be parameterized through three parameters: pulse amplitude, frequency, and temporal gradient. This paper investigates the hot-side system response to the pulse amplitude via detached eddy simulations (DES) of a turbocharger radial turbine system including the exhaust manifold. First, the computational model is validated against experimental data obtained in gas-stand flow conditions. Then, two different mass flow pulses, characterized by a pulse amplitude difference of ≈5%, are compared. An exergy-based post-processing approach shows the beneficial effects of increasing the pulse amplitude. An improvement of the turbine power by 1.3%, despite the increment of the heat transfer and total internal irreversibilities by 5.8% and 3.4%, respectively, is reported. As a result of the higher maximum speeds, internal losses caused by viscous friction are responsible for the growth of the total internal irreversibilities as pulse amplitude increases. [DOI: 10.1115/1.4053346]

Keywords: energy conversion/systems, energy systems analysis

1 Introduction

As the increasingly stringent regulations on gas emissions demand more efficient internal combustion engines (ICE), enhancing fuel economy and reducing gas emission is a popular topic in the automotive field nowadays. Among the different technologies, turbocharging, in conjunction with the so-called engine-downsizing, has been demonstrated as an effective and mature technology to achieve this goal.

Under on-engine operating conditions, the heat transfer and pulsating flow characterize the turbocharger behavior. Due to the compact nature of the system and the high temperatures of the exhaust gases, heat transfer occurs from the turbine to the compressor and the surroundings and may account for more than 20% of the total turbine power [1]. As consequence, the turbocharger operates as a diabatic machine. Rautenberg et al. [2], Rautenberg and Krammer [3], and Malobabic and Rautenberg [4] are among the pioneering researchers that rose the question of the effects of the heat transfer inside turbochargers. It is essential to account for the heat transfer effects to simulate reliable performance maps and improve turbocharger-engine matching. Indeed, since the heat transfer causes the temperature to be higher at the compressor outlet and lower at the turbine outlet, the temperature measurements cannot be used to calculate the power supplied or extracted. The higher temperature at the compressor outlet would be accounted as an apparent increase in the power consumption, decreasing the isentropic efficiency. On contrary, since the turbine power is inferred at the compressor stage, the turbine efficiency would appear larger. As result, the compressor performance is underestimated while the turbine one is overestimated, with the possibility for the isentropic efficiency to reach nonphysical values [5]. Different models accounting for the heat transfer effects have been proposed in the literature to predict the diabatic efficiency. The main differences rely on the authors' assumptions whether heat transfer occurs before or after the compression/expansion process [5,6]. The apparent effect influences the isentropic efficiency particularly at the lower characteristic speeds, where the difference is up to 20% for both compressor and turbine [6].

Nowadays, several authors have shown the detrimental impact of heat transfer on rotor efficiency, especially at low rotational speeds. Romagnoli and Martinez-Botas [7] reported an efficiency drop, from adiabatic to diabatic conditions, up to 30%. In an experimental campaign, Shaaban and Seume [8] registered a 55% turbine power decrease compared to adiabatic conditions, demonstrating the effectiveness of thermal insulation to increase the turbine power. On the numerical side, Lim et al. [9] reported a decrease of the turbine power up to 10%, for increasing levels of heat transfer, compared to adiabatic conditions.

Besides the heat transfer, the turbocharger turbine is subject to a pulsating flow. The radial turbine, essentially designed and optimized to operate under continuous flow, works in non-optimal conditions with deviations from the gas-stand performance. During the pulse cycle, the turbine shows performance deviations from gas-stand conditions, forming a hysteresis loop that is generally represented as mass flow parameter (MFP) against expansion ratio (π), or isentropic efficiency (η_{is}) against blade speed ratio (BSR). The area enclosed by the loop, a measure of the unsteadiness effects, is strongly dependent on the pulse shape, which can be parameterized through pulse amplitude, frequency, and temporal gradient. Pulse frequency was firstly pointed as the parameter driving the unsteady behavior of the turbine, with both experimental and numerical studies reporting an enlargement of the hysteresis loop with increasing pulse frequency [10–16]. Based on this observation, different criteria have been proposed in the literature to determine whether the turbine operates as a quasi-steady device or not. First, the Strouhal number was used to identify the passage from quasi-steady to unsteady behavior [17,18], but other forms based on it have been successively introduced. Szymko et al. [10] proposed a modified Strouhal number (MSt) accounting for the pulse length fraction. Then, Copeland et al. [19] introduced a Λ criterion to account for the pulse amplitude effects, subsequently reformulated by Cao et al. [13] to include instantaneous pressure variation effects. Aside from frequency, the pulse amplitude and shape profile affect the turbine unsteady behavior. It is demonstrated that

[1]Corresponding author.

Contributed by the Advanced Energy Systems Division of ASME for publication in the Journal of Energy Resources Technology. Manuscript received July 5, 2021; final manuscript received November 12, 2021; published online January 21, 2022. Assoc. Editor: Roberto Carapellucci.

increasing the pulse amplitude has the effect to enlarge the hysteresis loop [13–15,20]. This is motivated by the fact that the higher is the amplitude, the larger is the amount of mass flow which is found at a condition far from the cycle-averaged steady condition. Recently, Lee et al. [21] and Rezk et al. [22] investigated the effects of different pulse shapes on the turbine performance. In these numerical studies, the square profile was shown to have the largest detrimental effect on the turbine efficiency compared to realistic, sinusoidal, and triangular profiles.

A common approximation in the analysis of the turbine response to pulse amplitude is the overlapping between amplitude and temporal gradient effects [13–15,20]. Generally, in numerical studies, different pulse strategies are obtained by stretching or compressing the pulse shape to enlarge or reduce the pulse amplitude. If on one side this simplification is convenient, the major drawback results in the change of the pulse slope, so that the effects of both pulse amplitude and temporal gradient overlap. The methodology used in this work is different and aims to completely decouple the pulse amplitude and temporal gradient effects. Two different mass flow rate pulses, characterized by an amplitude difference equal to $\approx 5\%$ and the same temporal gradient, are compared. Then, an analysis of the hot-side system response to the pulse amplitude is carried to completion via an exergy-based post-processing method, which highlights the pulse amplitude effects in terms of turbine power, heat transfer, and entropy generation inside the different components of the hot-side: exhaust manifold, volute, and rotor.

2 Methodology

In this section, the computational model used is described and the validation study is reported. The system, represented in Fig. 1, consists of a single scroll and 12 blades turbine applied in a 2.0 L and four-cylinder engine passenger car. As the flow field inside the volute is largely affected by the system of the upstream bent pipes [23], the exhaust manifold is included in the model in order to replicate real on-engine conditions. Downstream to the turbine, the diffuser is followed by a convergent duct (not shown in Fig. 1) with the outlet boundary located at 13 rotor diameters ($D = 55$ mm) from the rotor-diffuser interface. This is meant to limit the direct effects of the boundary conditions imposed on the predicted flow field inside the rotor, which may result in a pressure damping at the rotor trailing edge [24].

2.1 Computational Setup. The governing equations represented by the conservation of mass, momentum, and energy are solved through the commercial solver STAR-CCM+ by Siemens. Since the flow is highly compressible and non-isothermal, a density-based coupled solver is chosen, so that the conservation equations are solved simultaneously. Air is considered as working fluid, while density and pressure are linked together by the ideal gas law ($p = \rho RT$). Furthermore, because of the large temperature gradients, the molecular dynamic viscosity μ is modeled according to Sutherland's law, while the specific heat at constant pressure c_p with a polynomial expression of the temperature.

Given the pulsating nature of the flow inside a turbocharger turbine, conditions of low and high mass flow rate alternate to each other during the engine cycle. As consequence, to handle both conditions, a detached eddy simulation (DES) is adopted. This hybrid approach has the advantage of resolving the near-wall region by a Reynolds-averaged Navier–Stokes (RANS) model, reducing the grid resolution needed at the wall, while an large eddy simulation (LES) approach is used in the separated and core regions. In the present work, the two-equation k-ω SST (shear stress transport) turbulence model by Menter [25] is used for the RANS computation, while the standard Smagorinsky subgrid-scale model for the LES [26]. Improved Delayed DES formulation (IDDES), formulated by Shur et al. [27], is adopted to handle the RANS-LES interface.

2.2 Boundary Conditions. The turbine response to the pulse amplitude is studied by comparing two different pulse profiles, derived accordingly to an experimentally-calibrated GT-POWER model, which reproduce two different exhaust valve strategies (hereinafter EVSs) at an engine operating point equal to 1500 rpm. A complete engine cycle comprises four pulses, one for each runner, according to the firing sequence 2-1-3-4 (with reference to Fig. 1).

As boundary conditions, time-varying mass flow rate and total temperature are imposed at the exhaust manifold inlets (see Fig. 2). Data are normalized by the maximum mass flow rate, $\dot{m}_{\max} = 0.19$ kg/s, and total temperature, $T_{t,\max} = 1609$ K, respectively. The mass flow rate amplitude difference between EVS1 (lower amplitude pulse) and EVS2 (higher amplitude pulse) is $\approx 5\%$, with EVS1 characterized by an earlier injection of mass to compensate for the difference in mass flow at the pulse peak. Moreover, to ensure the complete comparability between the two EVSs,

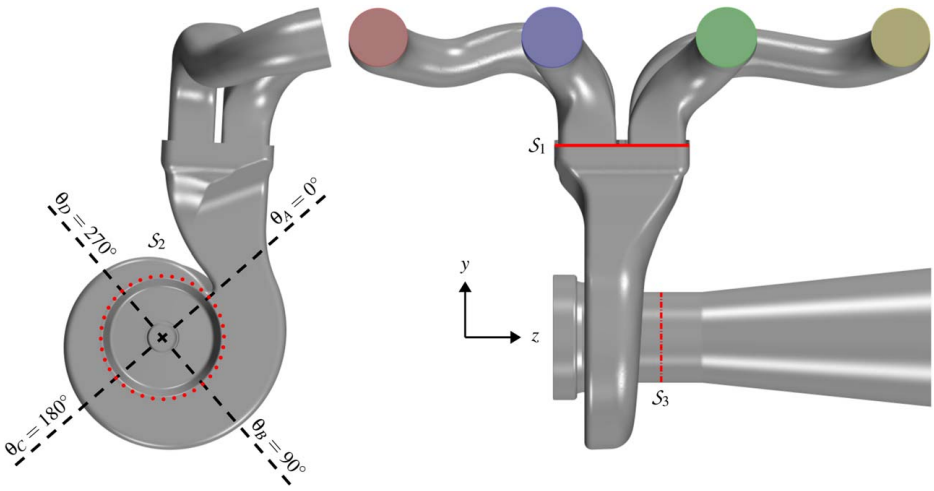

Fig. 1 Top (x – y plane) and lateral (y – z plane) views of the computational domain. The flow is injected through the exhaust manifold inlets according to the firing sequence 2-1-3-4 (with inlets numbered from left to right). The interfaces between components are highlighted and the volute sections at the circumferential positions $\theta_A = 0$ deg, $\theta_B = 90$ deg, $\theta_C = 180$ deg, and $\theta_D = 270$ deg are also reported.

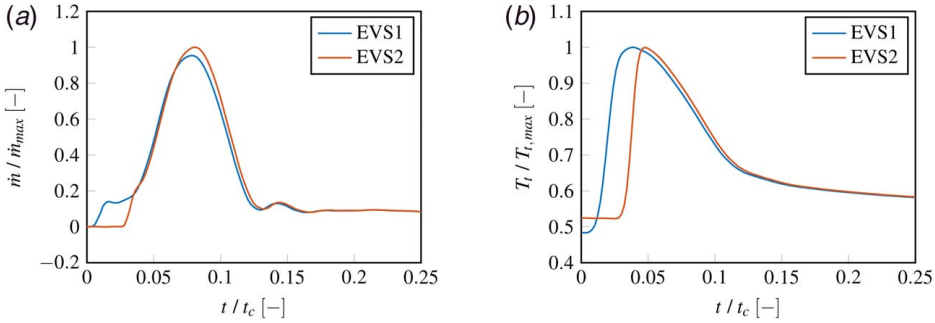

Fig. 2 Time-varying boundary conditions imposed at the exhaust manifold inlet. Axes are normalized by the engine period $t_c = 0.0799$ s, the maximum mass flow rate $\dot{m}_{max} = 0.19$ kg/s, and the maximum total temperature $T_{t,max} = 1609$ K: (*a*) mass flow rate and (*b*) total temperature.

the cycle-averaged inflow exergy is kept the same, so that the system response is not affected by a different maximum useful work possible. This represents a crucial point and a substantial difference with the previous literature studies, where constraints are imposed only on the cycle-averaged total pressure and temperature [13–15,20,28]. As pointed by Zhao et al. [28], this methodology leads to a degree of uncertainty, since different pulse profiles are characterized by a different isentropic expansion power at the turbine. The second factor of uncertainty in the previously reported research studies is the overlap of the pulse amplitude and frequency effects with the temporal gradients ones [13,19]. Here, due to the particular shape of the boundary conditions imposed, the pulse amplitude effects are decoupled from the temporal gradient ones, since the slope of the mass flow rate pulse is kept the same between EVSs. It is important to highlight that the imposed constraints on the cycle-averaged mass flow rate, inflow exergy, and temporal gradient are necessary to isolate the pulse amplitude effects and achieve a better characterization of the system response.

The second goal of the work is to assess the heat transfer response to the pulse amplitude. For this reason, walls are treated as smooth and diabatic with two different constant temperatures adopted: the first, $T_{w1} = 1073$ K, is imposed at the exhaust manifold and volute walls, the second, $T_{w2} = 930$ K, at the outlet pipe. Since the timescale associated with the solid material inertia is much larger than the pulse one [1], a constant temperature at the wall represents a realistic condition. On contrary, rotor surfaces are treated as adiabatic, since the fraction of heat transfer occurring in the rotor is negligible compared to the volute and diffuser [29].

At the outlet, time-varying static pressure and temperature are imposed accordingly to the GT-POWER model and represented in Fig. 3. The rotation of the rotor, characterized by a time-varying rotational speed equal to $\omega = 80812 \pm 2014$ rpm, is handled by the Sliding Mesh Method (SMM) so that the turbine is physically rotating at every time-step.

2.3 Validation Study. In order to validate the model, a steady-state RANS with the use of a multi-reference frame method (MRF) is used to compare the numerical results to the experimental data obtained in gas-stand experiments. To replicate the experimental setup, the computational domain is modified by substituting the exhaust manifold with a straight pipe 310 mm long. Adiabatic boundary conditions are imposed at the walls since, under gas-stand conditions, the expansion ratio has been demonstrated to not vary with respect to the type of boundary condition imposed [30]. Two different operating points are also studied through the DES model: the first is characterized by a similar rotational speed as for the pulsating flow cases, while the second represents an off-design point to assess the generality of the model. For the DES model, the sliding mesh method is used to handle the rotation of the turbine, with a time-step corresponding to 3 deg of rotation of the rotor.

Results are shown in Fig. 4, which presents the performance map in terms of mass flow parameter,

$$\mathrm{MFP} = \frac{\dot{m}\sqrt{T_t}}{p_t} \tag{1}$$

with quantities calculated at the inlet pipe-volute interface $\mathcal{S}_1$, and expansion ratio,

$$\pi = \frac{p_{t,in}}{p_{out}} \tag{2}$$

with the static pressure, p_{out}, calculated at the system outlet and equal to the atmospheric pressure. The numerical results show a good agreement with the experimental data, indicating a good accuracy for both the RANS and DES models. Indeed, the maximum percentage deviation between experimental and numerical results is registered below 3%.

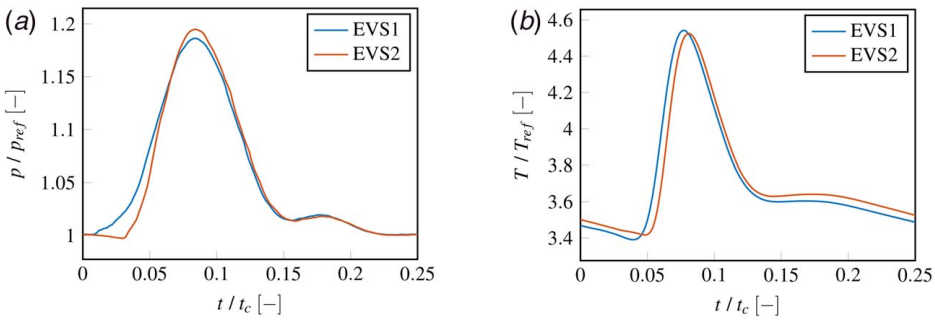

Fig. 3 Time-varying boundary conditions imposed at the outlet section. Axes are normalized by the engine period $t_c = 0.0799$ s, the reference static pressure $p_{ref} = 101.3$ kPa, and the reference static temperature $T_{ref} = 298.15$ K: (*a*) static pressure and (*b*) static temperature.

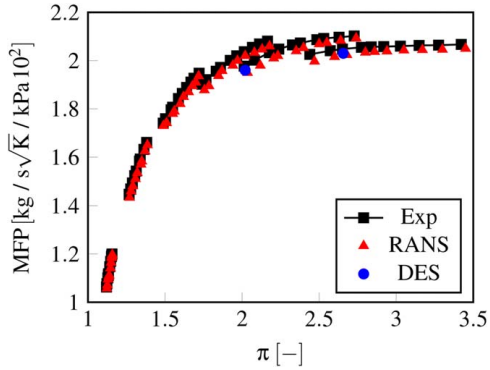

Fig. 4 Turbine performance map as mass flow parameter (MFP) against expansion ratio (π)

Fig. 5 Detailed view of the mesh inside the rotor at a section in the *x*–*y* plane

Since the target of the work is to investigate the response of the turbine power and heat transfer, wall resolution needs special attention. For this reason, the surface-averaged y_+ has been kept smaller than unity during pulsating flow conditions. For a detailed description of the mesh sensitivity study, the interested reader is referred to Ref. [31]. As final setup, the computational domain (see Fig. 5 for a detailed view of the mesh) is constituted by 22 M polyhedral elements distributed as in the following: 10% in the exhaust manifold, 32% in the volute, 35% in the rotor, and 23% in the outlet pipe. Downstream to the diffuser, in the outlet convergent duct, the grid is extruded and gradually stretched, since the flow is expected to be more aligned to the duct axis.

2.4 Post-Processing. In the post-processing phase, an exergy-based analysis is used to investigate the global system performance. The reader is referred to the existing literature for the application of the below-mentioned flow exergy methodology in turbomachinery applications (e.g., see Refs. [9,23,32]).

For a general open system, the specific exergy (in the reference frame of a given environment) is the maximum amount of shaft work per unit mass that can be extracted until the considered system is at thermal and mechanical equilibrium with the environment, i.e., the dead state. Mathematically, the specific exergy for a single-phase and non-reactive flow reads as

$$e_f = h_t(T_t) - h_o - T_o\left[s\left(T_t, p_t\right) - s_o\right] \tag{3}$$

where h and s represent the specific enthalpy and entropy, respectively, while the subscripts t and o denote the total quantity and the dead state, respectively. Here, the dead state is chosen as the ambient conditions ($T_o = 298.15$ K, $p_o = 101.3$ kPa), so that an evaluation of the theoretical maximum shaft work that could be extracted from the global system perspective is possible.

Exergy is never conserved and always destroyed during an irreversible process [33,34]. By accounting for all the exergy streams in and out of the system, the exergy destruction (or internal exergy loss), which is proportional to the entropy generation, can be determined using the exergy budget equation in Eq. (4).

$$\underbrace{\frac{d}{dt}\left[\iiint_{V^*(t)} (\rho e_f)\, \mathrm{d}V\right]}_{A} + \underbrace{\oiint_{S^*(t)} \left[\rho e_f \left\{(\vec{u} - \vec{u}_b)\cdot\vec{n}\right\}\right] \mathrm{d}S}_{-B} =$$
$$\underbrace{-\oiint_{S^*(t)} \left[\left(\vec{r}\times\vec{f}_{net}\right)\cdot\vec{\Omega}\right] \mathrm{d}S}_{C} \underbrace{-\oiint_{S^*(t)} \left[\left(1-\frac{T_o}{T_w}\right)(\vec{q}\cdot\vec{n})\right] \mathrm{d}S}_{D}$$
$$\underbrace{-T_o \dot{S}_{gen}}_{E} + \underbrace{\frac{d}{dt}\left[\iiint_{V^*(t)} p\, \mathrm{d}V\right]}_{F} \tag{4}$$

In Eq. (4), $\vec{u}$ is the velocity of a Lagrangian fluid particle, and $\vec{u}_b$ is the local velocity of the control surface $S^*(t)$ enclosing an arbitrary moving control volume $V^*(t)$. The outward normal vector of $S^*(t)$ is depicted by $\vec{n}$. $\vec{f}_{net}$, $\vec{r}$, $\vec{\Omega}$, and $\vec{q}$ represent the net force on the rotor surface per unit area vector, position vector, rotational speed vector and heat flux vector, respectively. Exergy can be transferred and destroyed through different physical mechanisms which, with reference to Eq. (4), are listed as follows:

(*A*) exergy local temporal rate of change in $V^*(t)$
(*B*) net flow exergy change as fluid particles advect through $S^*(t)$
(*C*) shaft power $\dot{W}_T$ across $S^*(t)$
(*D*) flow exergy transfer via heat transport across $S^*(t)$
(*E*) exergy destroyed via total internal irreversibilities in $V^*(t)$
(*F*) unsteady contribution in $V^*(t)$

A schematic representation of the exergy balance is also given in Fig. 6 for steady-state conditions. In a thermofluidic system, the presence of the internal irreversibilities (term *E*), together with the exergy transported by heat transfer (term *D*), reduces the maximum useful work possible, i.e., the exergetic content. It is, therefore, important to reduce the exergy losses caused by internal irreversibilities in order to maximize the available work [34].

The exergy losses caused by total internal irreversibilities (term *E*) can be evaluated by rearranging Eq. (4) as

$$E = -B - C - D - (A - F) \tag{5}$$

and by computing the different terms of the right-hand side numerically. However, this approach provides no information on the nature of the internal irreversibilities. Indeed, in a thermofluidic system as the one studied in the present work, entropy generation

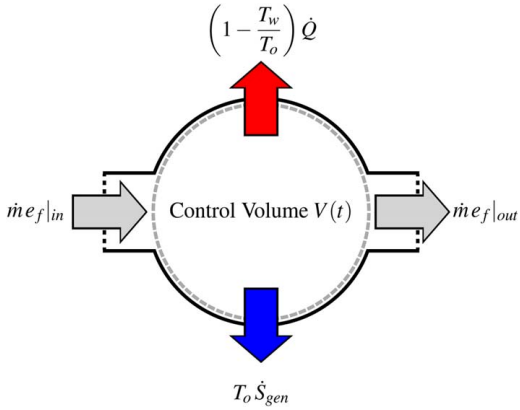

Fig. 6 Schematic sketch representing the exergy balance in steady-state conditions

is caused by both viscous friction and thermal conduction, as result of the velocity and temperature gradients in the flow field [35]. If the identification of the aerothermodynamic losses is of interest, as in the present work, the exergy losses can be directly computed by volume integration of the entropy generation rate caused by the viscous ($\dot{S}_{gen,\,viscous}$) and thermal ($\dot{S}_{gen,\,thermal}$) mechanisms as in Eq. (6).

$$\dot{S}_{gen} = \underbrace{\iiint_{V^*(t)} \left[\frac{\mu_{eff}}{T} \left(2\, S_{ij}\, S_{ij} - \frac{2}{3}\, S_{kk}\, S_{kk} \right) \right] \mathrm{d}V}_{\dot{S}_{gen,\,viscous}} + \underbrace{\iiint_{V^*(t)} \left[\frac{k_{eff}}{T^2} \left(\frac{\partial T}{\partial x_j} \right)^2 \right] \mathrm{d}V}_{\dot{S}_{gen,\,thermal}} \tag{6}$$

Here, S_{ij} is the strain rate tensor, i.e., the symmetric part of the velocity gradient tensor $\partial u_i/\partial x_j$, while μ_{eff} and k_{eff} represent the effective dynamic viscosity and thermal conductivity, respectively, sum of the molecular and turbulent ones.

The two approaches for computing the entropy generation proposed in Eqs. (5) and (6) are named indirect and direct method, respectively [36]. If the direct method has the advantage of distinguishing among the different aerothermodynamic mechanisms of entropy generation, it is more resources demanding, since it involves volume integration. As consequence, the results are particularly sensitive to the spatial discretization of the domain besides the turbulence model adopted [9,37]. In the present work, the direct method for the computation of the entropy generation is chosen, as the aim is to achieve a complete characterization of the aerothermodynamic losses response to the pulse amplitude. To account for the relative importance between the viscous and thermal irreversibilities, the Bejan number [38,39],

$$Be = \frac{1}{1 + \dfrac{\dot{S}_{gen,viscous}}{\dot{S}_{gen,thermal}}} \tag{7}$$

is considered. Bejan number ranges from 0, when irreversibilities are driven by viscous mechanisms, to 1, when thermal effects are dominant.

The use of the concept of exergy as a post-processing tool is rapidly growing in turbocharger applications [9,30,31,40–42]. However, in the present work, exergy assumes an important role in the pre-processing phase, since it represents a constraint for the design of the pulses. Indeed, when pulse parametric studies are conducted, it is of particular importance for the boundary conditions to be characterized by the same cycle-averaged inflow exergy. In this way, the turbine response, as well as the exergy losses, is not influenced by a different maximum useful work available inside the system.

3 Results

In order to ensure a proper initialization of the flow field, simulations are run for a total of two engine cycles, with statistics calculated by excluding the first one. Percentage differences between EVSs reported in the following are calculated according to the formula $\Delta\phi = (\phi_{EVS2} - \phi_{EVS1})/\phi_{EVS1}$, with ϕ a generic quantity of interest.

3.1 Exergy Budget. The exergy budget and Bejan number are depicted for both EVSs in Figs. 7(*a*) and 7(*b*), respectively, with reference to the single components of the domain. Exergy budget data are normalized by the cycle-averaged inflow exergy, $\dot{m}\, e_f$, calculated at the exhaust manifold inlet. Normalization is performed for purpose of clearness and, since the cycle-averaged inflow exergy is kept the same between EVSs, results do not change qualitatively. From Fig. 7(*a*), it is worth highlighting that only $\approx 12\%$ of the total available exergy is converted into mechanical work, while the remaining $\approx 80\%$ is still available downstream to the turbine after the expansion process. The remaining exergetic content, lost via heat transfer and total internal irreversibilities, accounts for a consistent fraction, $\approx 8\%$, of the cycle-averaged inflow exergy. The unsteady terms in the exergy budget (terms A and F with reference to Eq. (4)) are not represented because negligible compared to the others. Exergy accumulation (term A) is null during the entire engine cycle, while the pressure time derivative contribution (term F) is negligible because of the symmetry of the pulse.

In the following, the different terms of the exergy budget as turbine power, heat transfer, and exergy losses via internal viscous and thermal irreversibilities are analyzed by considering their response to the pulse amplitude through their evolution in time.

3.1.1 Turbine Performance. The major result from the exergy budget in Fig. 7(*a*) relies on the increment of the turbine power as amplitude increases. Although Fig. 7(*a*) and Table 1 highlight the turbine power as the least sensible exergy budget term among all, a +1.3% percentage difference is still significant in terms of turbine performance. The growth of the turbine power is even more significant when considering that, at the turbine inlet, the inflow exergy is smaller for EVS2 compared to EVS1. Indeed, exergy losses, caused by both heat transfer and internal irreversibilities, increase with increasing pulse amplitude in both the exhaust manifold and volute, reducing the useful work at the turbine inlet from EVS1 to EVS2 (see Fig. 7(*a*) and Table 1).

For a better understanding of the turbine performance, it is useful to relate the cycle-averaged turbine power to the instantaneous expansion ratio during the pulse cycle (see Fig. 8(*a*)). Here, the inlet total pressure is calculated at section $\mathcal{S}_1$ and the outlet static pressure at section $\mathcal{S}_3$ (with reference to Fig. 1). With increasing pulse amplitude from EVS1 to EVS2, the maximum expansion ratio increases, with a percentage difference equal to +3.0%

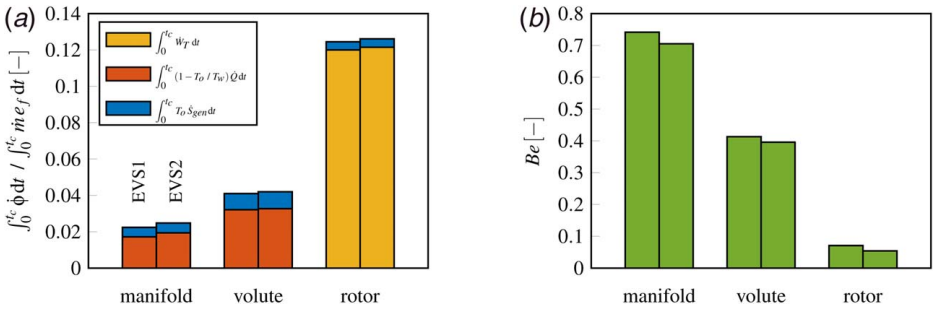

Fig. 7 Pulse amplitude effects on the exergy budget and Bejan number on the different components of the system: exhaust manifold, volute, and rotor. Exergy budget data are normalized by the cycle-averaged inflow exergy, $\dot{m}\, e_f$, at the exhaust manifold inlet: (*a*) exergy budget and (*b*) Bejan number.

Table 1 Cycle-averaged values of the turbine power (term C), exergy lost by heat transfer (term D), and exergy losses via total internal irreversibilities (term E) at the exhaust manifold, volute, and rotor, respectively

	Manifold		Volute		Rotor		Irreversibilities	
	D [W]	E [W]	D [W]	E [W]	C [W]	E [W]	$T_o\,\dot{S}_{gen,viscous}$ [W]	$T_o\,\dot{S}_{gen,thermal}$ [W]
EVS1	637	193	1191	330	4455	167	471	219
EVS2	722	197	1213	346	4512	171	505	209
$\Delta\phi$ [%]	+13.3%	+2.1%	+1.8%	+4.8%	+1.3%	+2.4%	+7.2%	−4.6%

Note: Viscous and thermal irreversibilities for the entire system are also reported.

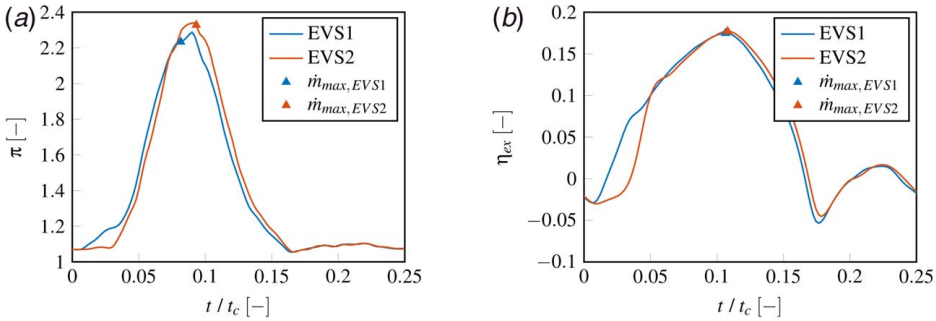

Fig. 8 Pulse amplitude effects on the time-varying expansion ratio and exergy utilization during the pulse cycle. The instants of maximum mass flow rate are also highlighted: (*a*) expansion ratio and (*b*) exergy utilization.

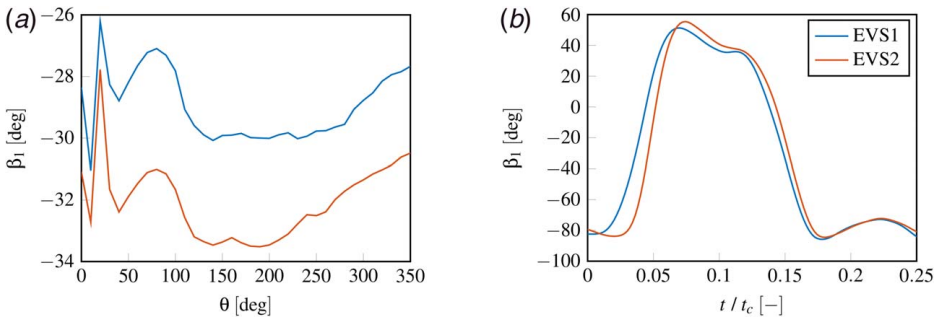

Fig. 9 Pulse amplitude effects on the relative inflow angle. The cycle-averaged and the circumferentially-averaged relative inflow angles are plotted against the circumferential position and the normalized time, respectively: (*a*) cycle-averaged relative inflow angle and (*b*) instantaneous relative inflow angle.

at the pulse peak, as a result of the larger local MFP values. A smaller increment, equal to +0.3%, is registered as well for the cycle-averaged expansion ratio, showing the beneficial effects of a higher pulse amplitude on both the instantaneous and cycle-averaged expansion capacity of the turbine. From Fig. 8(*a*), it is also interesting to notice that the shape of the expansion ratio curve, during the acceleration and deceleration phases, is similar for both EVSs. This is justified by the constraint on the temporal gradient of the mass flow rate pulses imposed as boundary condition (see Fig. 2(*a*)). As consequence, besides the peak, the only difference relies on the early part of the pulse period, where EVS1 experiences larger expansion ratio values due to an earlier injection of mass compared to EVS2.

The second parameter of interest to assess the turbine response to the pulse amplitude is the exergy utilization,

$$\eta_{ex} = \frac{\dot{W}_T}{\dot{m}\, e_f} \tag{8}$$

defined as the ratio between the turbine power and the inflow exergy (calculated at section $\mathcal{S}_2$) which is reported in Fig. 8(*b*) during the pulse cycle. As for the instantaneous expansion ratio, both the EVSs experience a very similar trend. At the beginning of the acceleration phase and the end of the deceleration phase, exergy utilization assumes negative values. In these conditions, the mass flow rate filling the turbine is particularly low, so that a freewheel condition is reached. As consequence, the transfer of momentum occurs from the turbine to the flow, resulting in negative values of the turbine torque. During the acceleration phase, exergy utilization rapidly increases until its maximum value, occurring close to the maximum mass flow rate at the turbine inlet. Here, EVS1 experiences a lower maximum exergy utilization, with a percentage difference between EVS1 and EVS2 equal to +1.3%. Then, after the point of maximum efficiency, the exergy utilization drops rapidly to negative values at the end of the deceleration phase. The results highlight that increasing the pulse amplitude has beneficial effects on both the maximum and cycle-averaged exergy utilization, which is reported equal to $\eta_{ex,EVS1} = 0.126$ and $\eta_{ex,EVS2} = 0.129$ for EVS1 and EVS2, respectively.

The increment of the turbine power with increasing pulse amplitude was already observed by Zhao et al. [28] on the high pressure turbine (HPT) of a two-stage turbocharger system. However, together with the increase of the turbine power, a decrease of the isentropic efficiency, whose definition is reported in Eq. (A1) in

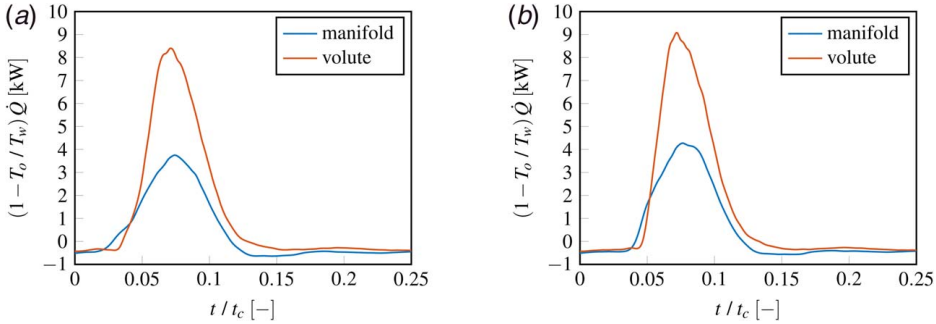

Fig. 10 Time-varying exergy lost by heat transfer during the pulse cycle at the exhaust manifold and volute walls: (*a*) EVS1 and (*b*) EVS2

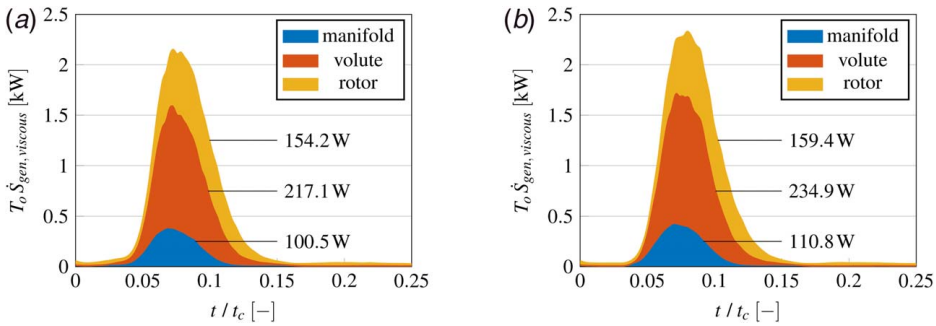

Fig. 11 Time-varying exergy losses via viscous mechanisms during the pulse cycle: (*a*) EVS1 and (*b*) EVS2

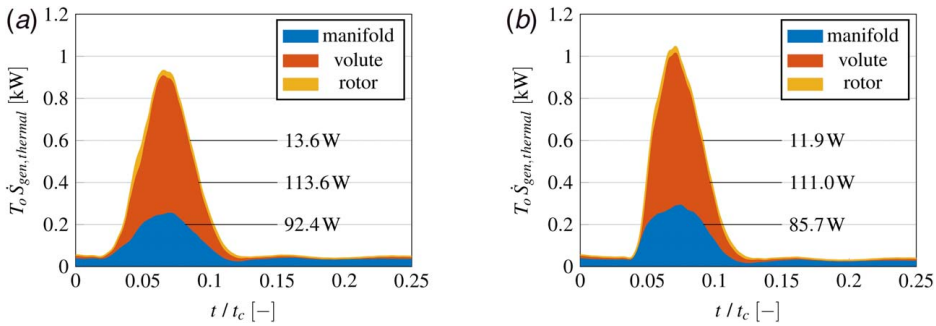

Fig. 12 Time-varying exergy losses via thermal mechanisms during the pulse cycle: (*a*) EVS1 and (*b*) EVS2

Appendix A, was reported. This apparent inconsistency shows that the isentropic efficiency is not a suitable quantity for comparisons of the turbine performance subject to different pulse profiles. If on one side it enables to determine how far the turbine operates from an ideal isentropic expansion, on the other it fails to provide a characterization of the turbine response to the pulse parameter studied. Indeed, the isentropic expansion power may be different for different pulse profiles, as well as the amount of entropy that can be generated. On contrary, the exergy utilization, which represents the fraction of the maximum useful power converted into mechanical power, offers a better understanding, especially if the amount of inflow exergy (the denominator of Eq. (8)) is kept the same. Moreover, it is important to highlight that a constant isentropic expansion power cannot be imposed through proper boundary conditions, since its definition includes the expansion ratio π, which is known in the aftermath.

The turbine aerodynamic performance are determined by the relative inflow angle, defined as the angle between the relative velocity of the flow and the meridional direction (for a schematic sketch see Fig. 13 in Appendix B). Depending on the relative inflow angle, the flow may separate on the turbine blade pressure side for negative β_1 values, or on the suction side for positive β_1 values, respectively. As consequence, the optimum range for β_1 is described to be between −30 deg and −20 deg, such that the secondary flows caused by the flow separation, as well as the entropy generated, are suppressed [43]. Padzillah et al. [43] showed that, with increasing frequency, the relative inflow angle spans within a more restricted range during the pulse cycle. Yang et al. [44] linked the instantaneous absolute inflow angle to the time derivative of the ratio between static pressure and temperature, besides the geometric parameters of the volute. Lim et al. [23] reported the exhaust manifold to have a direct effect on the inflow angle, as responsible for the secondary flows inside the volute.

In this work, the relative inflow angle β_1 has been measured by means of a series of 36 stationary probe points, circumferentially distributed around the rotor, at a distance equal to 2 mm from the blade

leading edge. The cycle-averaged inflow angle is reported in Fig. 9(*a*) against the circumferential position. For both EVSs, it can be noticed that β_1 relies, on average, close to the optimum range. However, Fig. 9(*b*), which represents the instantaneous circumferentially-averaged relative inflow angle, shows that β_1 experiences a wide range of values during the pulse cycle. At low mass flow rates, the relative inflow angle assumes large negative values, as the circumferential velocity of the blade is larger compared to the flow. This condition corresponds to negative values of the turbine torque and exergy utilization (see Fig. 8(*b*)). With increasing mass flow rate during the acceleration phase, β_1 grows until the mass flow rate peak is reached. Here, EVS2 experiences larger relative inflow angles compared to EVS1, as result of higher circumferential velocities (note that the rotor speed is the same). The maximum relative inflow angle is reported equal to 48 deg and 51 deg for EVS1 and EVS2, respectively. The results show that a higher pulse amplitude gives rise to larger instantaneous inflow angles at the pulse peak, but not necessarily on average. It is also important to notice that, instantaneously, the relative inflow angle spans within the optimum range for only the 2.4% of the pulse duration at moderate mass flow rates, where the useful work is low. As consequence, the radial turbine works in severe off-design aerodynamic conditions for the large duration of the engine cycle.

3.1.2 Heat Transfer. Globally, the exergy lost by heat transfer accounts for ≈5% of the cycle-averaged inflow exergy, with the volute responsible for ≈65% of the total. As reported in Fig. 7(*a*) and Table 1, exergy lost by heat transfer shows an ascending trend with increasing pulse amplitude in both the exhaust manifold and volute. Percentage differences, equal to +13.3% and 1.8% (see Table 1), demonstrate a significant influence of the pulse amplitude on heat transfer, especially at the exhaust manifold. With increasing pulse amplitude, the growth of heat transfer is partially determined by the mass flow-averaged temperature which, by considering one single runner inlet, is equal to $T_{EVS1} = 1227$ K and $T_{EVS2} = 1232$ K. The large sensitivity of the heat transfer inside the exhaust manifold, +13.3%, derives from the stronger effects of the boundary conditions at the inlet of the system. Indeed, as the flow travels through the different components, the temperature difference between the fluid and the walls decreases. As consequence, the temperature difference between the two EVSs is smaller at the exhaust manifold-volute interface compared to the exhaust manifold inlet.

In Fig. 10, the time-varying exergy lost by heat transfer is reported during the pulse cycle for both the exhaust manifold and volute. It can be noticed how the heat transfer rate is larger at the pulse peak for EVS2 compared to EVS1, highlighting a remarkable influence of the pulse amplitude on the heat transfer. During the intra-pulse phase, heat transfer is otherwise reversed, directed from the surrounding to the domain, as result of the low mass flow rates and temperatures occurring.

3.1.3 Internal Irreversibilities. The total internal irreversibilities, sum of the viscous and thermal ones, account for a small but significant fraction, ≈ 2%, of the cycle-averaged inflow exergy. With increasing pulse amplitude, the entropy generation increases in all the hot-side components (see Fig. 7(*a*) and Table 1) with the largest variation, equal to +5%, occurring inside the volute, which is responsible for the largest fraction, ≈ 50%, of the total internal irreversibilities.

A deeper understanding of the nature of entropy generation is given by the Bejan number, represented in Fig. 7(*b*), which experiences a descending trend in all the hot-side components as the pulse amplitude increases. This trend highlights that entropy generation associated with viscous mechanisms increases compared to thermal irreversibilities. This is justified by the fact that viscous effects, proportional to the velocity gradients, are larger with increasing pulse amplitude, which determines the maximum velocity at the domain boundaries. At the exhaust manifold inlets, the maximum velocity for EVS1 ($U_{max,EVS1} = 363$ m/s) is reported to be smaller compared to EVS2 ($U_{max,EVS2} = 373$ m/s). Inside the rotor, the Bejan number assumes smaller values compared to the exhaust manifold and volute, both as the flow field is dominated by the viscous effects, i.e., larger velocity gradients caused by the high rotational speed of the rotor, and the adiabatic boundary condition imposed at the wall.

The temporal evolution of the exergy losses caused by viscous entropy generation is reported in Fig. 11 during the pulse cycle. Although the trend looks similar for both EVSs during the pulse phase, EVS2 is characterized by a higher peak. Here, the percentage variation is reported equal to +8.3%, showing a remarkable influence of the pulse amplitude. Globally, viscous irreversibilities increase by +7.2% from EVS1 to EVS2 (see Table 1) while percentage differences in the different components of the hot-side system are reported equal to +10.3%, +8.2%, and +3.4% for the exhaust manifold, volute, and rotor, respectively. As for the exergy lost by heat transfer, it is worth noticing that the effects of the boundary conditions reduce as the flow travels through the different components of the system.

As reported in Table 1, the exergy losses caused by thermal irreversibilities decrease with increasing pulse amplitude from EVS1 to EVS2. Despite this trend, the evolution in time of the thermal irreversibilities, given in Fig. 12, shows that EVS2 is characterized by a higher peak than EVS1 (compare Figs. 12(*a*) and 12(*b*)) with a percentage difference equal to +12.1% at the pulse peak. Moreover, as already observed by the Bejan number in Fig. 7(*b*), the exergy losses caused by thermal irreversibilities are particularly small inside the rotor, where they account for only ≈ 6% of the total.

4 Conclusions

The present work investigates the effects of the mass flow rate pulse amplitude on the turbine performance, as well as the impact on heat transfer and entropy generation, in a turbocharger radial turbine under engine-like conditions. Two different mass flow pulses, characterized by a difference in amplitude equal to ≈ 5% and the same cycle-averaged mass flow rate, inflow exergy, and temporal gradient are compared by means of an exergy-based post-processing approach.

The results presented highlight an important conclusion on the turbine performance:

- With increasing pulse amplitude, the turbine power improves by +1.3% despite the growth of the exergy losses caused by heat transfer and total internal irreversibilities, which limits further improvement.

The turbine performance are directly linked to the expansion ratio and exergy utilization. As amplitude increases, the maximum expansion ratio grows by +3.0% as result of larger local MFP values. A smaller increment, equal to +0.3%, is otherwise registered for the cycle-averaged value. The results show that increasing pulse amplitude has beneficial effects on both the instantaneous and cycle-averaged turbine performance. A similar trend is observed for the exergy utilization, which provides a better understanding of the turbine performance compared to the isentropic efficiency when different pulsating conditions are compared. Since exergy utilization is defined as the fraction of maximum useful power converted into mechanical power, it depends only on quantities upstream of the turbine. As consequence, proper boundary conditions can be defined to provide the same maximum useful work possible into the system. In this way, the system response (in terms of turbine power and total internal irreversibilities) is not affected by a different maximum useful work possible, a necessary condition to properly compare different pulse profiles and completely isolate the effects of the pulse characteristics. On contrary, it is not possible to impose the isentropic power through proper boundary conditions, since its definition includes the expansion ratio term, which is known in the aftermath.

The aerodynamic performance of the turbine are evaluated by analyzing the effects of the pulse amplitude on the relative inflow angle β_1. The results show that

- The relative inflow angle relies within the optimum range for a short duration of the pulse cycle, when the mass flow rate and the useful work are low.

As consequence, the turbine operates in severe off-design aerodynamic conditions for the large duration of the pulse cycle. Moreover,

- Increasing pulse amplitude gives rise to larger maximum relative inflow angles so that, during the pulse cycle, β_1 relies within a wider range of values.

This is related to the larger circumferential velocity of the flow at the pulse peak, since the rotational speed of the rotor is kept fixed between the EVSs.

The heat transfer and internal irreversibilities responses to pulse amplitude variations are object of study as well. Results demonstrate that

- As the pulse amplitude increases, the exergy lost by heat transfer is larger in both the exhaust manifold and volute, where the percentage differences are reported equal to +13.3% and +1.8%, respectively.

The influence of the pulse amplitude is particularly strong at the system inlet while it is mitigated as the flow travels through the different components of the system. Indeed, the temperature differences between the flow and the walls gradually diminish. The use of the so-called direct method for computing the entropy generation highlights that

- With increasing pulse amplitude, total internal irreversibilities grow in all the hot-side components as result of larger losses due to viscous friction.

Entropy generation caused by viscous irreversibilities is reported to increase due to the larger maximum velocities, which are determined by the pulse amplitude.

In this work, a particular focus is given on the concept of exergy, considered a suitable tool to investigate the turbine performance under different pulsating flow conditions. Indeed, in order to achieve a proper characterization of the system response to different pulse characteristics, the same maximum useful work possible, i.e., exergy content, should be imposed through proper boundary conditions. Under such constraint, the turbine performance, as well as the entropy generation, are correctly assessed. This aspect limits the understanding of previous literature studies on pulse amplitude and frequency effects. Based on the boundary conditions imposed, which enforce constraints on the temporal gradient and cycle-averaged inflow exergy, this study proposes a characterization of the pulse amplitude effects on a radial turbocharger turbine free of uncertainties related to changes of the temporal gradient and maximum useful work content.

Acknowledgment

This study was conducted within the Competence Center for Gas Exchange (CCGEx) at KTH. The authors would like to acknowledge the Swedish Energy Agency and CCGEx's industrial partners for their support and contributions. The support from EU project VISION-xEV, which has received funding from the European Union's Horizon 2020 research and innovation program under Grant Agreement No. 824314 is acknowledged by S.M. Lim and M. Mihaescu. We acknowledge that the results of this research have been achieved using KTH PDC under the Swedish Computing Infrastructure (SNIC) and the DECI resource Mahti based in Finland at CSC with support from the Partnership for Advanced Computing in Europe (PRACE) aisbl.

Conflict of Interest

There are no conflicts of interest.

Data Availability Statement

Data provided by a third party listed in Acknowledgment.

Nomenclature

h = specific enthalpy, J/kg
k = thermal conductivity, W/m K
p = pressure, Pa
s = specific entropy, J/kg K
t = time, s
D = diameter, m
R = ideal gas constant, J/kg K
S = surface area, m^2
T = temperature, K
V = volume, m^3
c_1 = absolute velocity, m/s
$c_{\theta 1}$ = absolute circumferential velocity, m/s
c_m = meridional velocity, m/s
c_p = specific heat at constant pressure, J/kg K
e_f = specific exergy, J/kg
u_1 = circumferential velocity, m/s
w_1 = relative velocity, m/s
$w_{\theta 1}$ = relative circumferential velocity, m/s
w_{m1} = relative meridional velocity m/s
y_+ = non-dimensional wall distance
$\dot{m}$ = mass flow rate, kg/s
$\vec{f}$ = force per unit area, N/m^2
$\vec{n}$ = unit normal vector
$\vec{q}$ = heat flux vector, W/m^2
$\vec{r}$ = position vector, m
$\vec{u}$ = Lagragian fluid particle velocity, m/s
$\dot{Q}$ = heat transfer rate, W
$\dot{S}_{gen}$ = entropy generation rate, W/K
$\dot{W}_T$ = turbine power, W
Be = Bejan number
MSt = modified Strouhal number

Greek Symbols

α_1 = absolute inflow angle, deg
ω = angular velocity, rad/s
θ = circumferential position, deg
ρ = density, kg/m^3
π = expansion ratio
η_{ex} = exergy utilization
ϕ = generic quantity
γ = heat capacity ratio
η_{is} = isentropic efficiency
Λ = Lambda criterion
μ = molecular dynamic viscosity, Pa s
β_1 = relative inflow angle, deg
$\vec{\Omega}$ = rotational speed vector, rad/s
τ = turbine torque, Nm

Superscripts and Subscripts

c = cycle
eff = effective
gen = generation
in = inlet
max = maximum
o = dead state
out = outlet
ref = reference

t = total quantity
w = wall

Appendix A: Isentropic Efficiency

The isentropic efficiency is defined as

$$\eta_{is} = \frac{\dot{W}_T}{\dot{m}\, c_p\, T_t \left(1 - \pi^{\frac{1-\gamma}{\gamma}}\right)} \tag{A1}$$

with $\dot{W}_T$ the turbine power, defined as the product between the turbine torque τ and the angular speed ω, $\dot{m}$ and T_t the mass flow rate at total temperature at the inlet section, respectively, π the expansion ratio, and γ the heat capacity ratio.

Appendix B: Turbine Velocity Triangles

Figure 13 shows a schematic representation of the velocity triangles at the turbine inlet. The different velocity vectors are reported as follows:

c_1: absolute velocity
c_m: meridional velocity component
$c_{\theta 1}$: absolute circumferential velocity component
w_1: relative velocity
w_{m1}: relative meridional velocity component
$w_{\theta 1}$: relative circumferential velocity component
u_1: circumferential velocity

The absolute and relative inflow angles α_1 and β_1 are defined as the angles between the absolute and the relative velocity vectors and the meridional direction, respectively. The relative inflow angle is negative when the relative circumferential velocity component $w_{\theta 1}$ is negative, or the absolute circumferential velocity component $c_{\theta 1}$ is smaller than the circumferential velocity u_1.

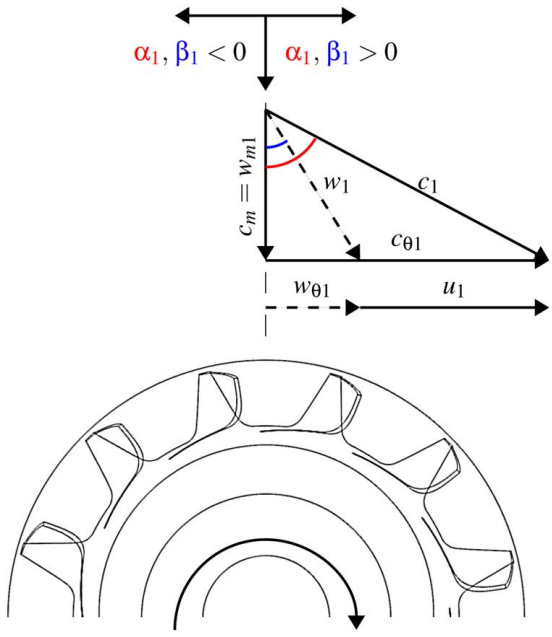

Fig. 13 Schematic sketch of the inflow velocity triangles

References

[1] Burke, R., Vagg, C., Chalet, D., and Chesse, P., 2015, "Heat Transfer in Turbocharger Turbines Under Steady, Pulsating and Transient Conditions," Int. J. Heat and Fluid Flow, **52**(4), pp. 185–197.
[2] Rautenberg, M., Malobabic, M., and Mobarak, A., 1984, "Influence of Heat Transfer Between Turbine and Compressor on the Performance of Small Turbochargers." In 1983 Tokyo International Gas Turbine Congress, Tokyo, Japan, Oct. 23–29, 1983, Proceedings. Volume 2 (A85-41776 20-07). Tokyo, Gas Turbine Society of Japan, 1984, pp. 567–574.
[3] Rautenberg, M., and Kammer, N., 1984, "On the Thermodynamics of Non-Adiabatic Compression and Expansion Process in Turbomachines," ICMPE, Proceedings of the 5th International Conference for Mechanical Power Engineering, Cairo, Egypt.
[4] Malobabic, M., and Rautenberg, M., 1987, "Adiabatic and Non-Adiabatic Efficiencies of Small Turbochargers," International Gas Turbine Congress, Tokyo, Japan, Oct, pp. 26–31.
[5] Romagnoli, A., Manivannan, A., Rajoo, S., Chiong, M., Feneley, A., Pesiridis, A., and Martinez-Botas, R., 2017, "A Review of Heat Transfer in Turbochargers," Renewable. Sustainable. Energy Rev., **79**(7), pp. 1442–1460.
[6] Sirakov, B., and Casey, M., 2013, "Evaluation of Heat Transfer Effects on Turbocharger Performance," ASME J. Turbomach., **135**(2), p. 021011.
[7] Romagnoli, A., and Martinez-Botas, R., 2012, "Heat Transfer Analysis in a Turbocharger Turbine: An Experimental and Computational Evaluation," Appl. Therm. Eng., **38**, pp. 58–77.
[8] Shaaban, S., and Seume, J., 2012, "Impact of Turbocharger Non-Adiabatic Operation on Engine Volumetric Efficiency and Turbo Lag," Int. J. Rotating Machinery, **2012**(4), p. 1.
[9] Lim, S. M., Dahlkild, A., and Mihaescu, M., 2018, "Aerothermodynamics and Exergy Analysis in Radial Turbine With Heat Transfer," ASME J. Turbomach., **140**(9), p. 091007.
[10] Szymko, S., Martinez-Botas, R., and Pullen, K., 2005, "Experimental Evaluation of Turbocharger Turbine Performance Under Pulsating Flow Conditions," ASME Turbo Expo 2005: Power for Land, Sea, and Air, Reno, NV, June 6–9.
[11] Copeland, C. D., Martinez-Botas, R., and Seiler, M., 2012, "Unsteady Performance of a Double Entry Turbocharger Turbine With a Comparison to Steady Flow Conditions," ASME J. Turbomach., **134**(2), p. 021022.
[12] Galindo, J., Fajardo, P., Navarro, R., and García-Cuevas, L., 2013, "Characterization of a Radial Turbocharger Turbine in Pulsating Flow by Means of Cfd and Its Application to Engine Modeling," Appl. Energy., **103**, pp. 116–127.
[13] Cao, T., Xu, L., Yang, M., and Martinez-Botas, R. F., 2014, "Radial Turbine Rotor Response to Pulsating Inlet Flows," ASME J. Turbomach., **136**(7), p. 071003.
[14] Ding, Z., Zhuge, W., Zhang, Y., Chen, H., and Martinez-Botas, R., 2017, "Investigation on Pulsating Flow Effect of a Turbocharger Turbine," ASME 2017 Fluids Engineering Division Summer Meeting, Waikoloa, HI, July 30–Aug. 3.
[15] Zhao, R., Li, W., Zhuge, W., Zhang, Y., Yin, Y., and Wu, Y., 2018, "Characterization of Two-stage Turbine System Under Steady and Pulsating Flow Conditions," Energy, **148**(12), pp. 407–423.
[16] Piscaglia, F., Onorati, A., Marelli, S., and Capobianco, M., 2019, "A Detailed One-Dimensional Model to Predict the Unsteady Behavior of Turbocharger Turbines for Internal Combustion Engine Applications," Int. J. Engine Res., **20**(3), pp. 327–349.
[17] Chen, H., and Winterbone, D., 1990, "A Method to Predict Performance of Vaneless Radial Turbines Under Steady and Unsteady Flow Conditions." *IMechE Turbocharging and Turbochargers, Paper(C405/008)*, pp. 13–22.
[18] Chen, H., Hakeem, I., and Martinez-Botas, R., 1996, "Modelling of a Turbocharger Turbine Under Pulsating Inlet Conditions," Proc. Inst. Mech. Eng., Part A: J. Power Energy, **210**(5), pp. 397–408.
[19] Copeland, C., Newton, P., Martinez-Botas, R., and Seiler, M., 2012, "A Comparison of Timescales Within a Pulsed Flow Turbocharger Turbine," 10th International Conference on Turbochargers and Turbocharging, London, UK.
[20] Yang, M., Deng, K., Martines-Botas, R., and Zhuge, W., 2016, "An Investigation on Unsteadiness of a Mixed-Flow Turbine Under Pulsating Conditions," Energy Convers. Manage., **110**(1), pp. 51–58.
[21] Lee, S. P., Rezk, A., Jupp, M., and Nickson, K., 2018, "The Influence of Pulse Shape on the Performance of a Mixed Flow Turbine for Turbocharger Applications," Int. J. Mech. Eng. Rob. Res., **7**(2), pp. 136–142.
[22] Rezk, A., Sharma, S., Barrans, S., Hossain, A. K., Lee, S. P., and Imran, M., 2021, "Computational Study of a Radial Flow Turbine Operates Under Various Pulsating Flow Shapes and Amplitudes," ASME J. Energy Resour. Technol., **143**(12), p. 120904.
[23] Lim, S. M., Dahlkild, A., and Mihaescu, M., 2019, "Influence of Upstream Exhaust Manifold on Pulsatile Turbocharger Turbine Performance," ASME J. Eng. Gas Turbines Power, **141**(6), p. 061010.
[24] Palfreyman, D., and Martinez-Botas, R., 2005, "The Pulsating Flow Field in a Mixed Flow Turbocharger Turbine: An Experimental and Computational Study," ASME J. Turbomach., **127**(1), pp. 144–155.
[25] Menter, F. R., 1994, "Two-equation Eddy-Viscosity Turbulence Models for Engineering Applications," AIAA. J., **32**(8), pp. 1598–1605.
[26] Smagorinsky, J., 1963, "General Circulation Experiments With the Primitive Equations: I. The Basic Experiment," Mon. Weather Rev., **91**(3), pp. 99–164.
[27] Shur, M. L., Spalart, P. R., Strelets, M. K., and Travin, A. K., 2008, "A Hybrid RANS-LES Approach With Delayed-des and Wall-Modelled LES Capabilities," Int. J. Heat and Fluid Flow, **29**(6), pp. 1638–1649.
[28] Zhao, R., Li, W., Zhuge, W., and Zhang, Y., 2019, "Unsteady Flow Loss Mechanism and Aerodynamic Improvement of Two-Stage Turbine Under Pulsating Conditions," Entropy, **21**(10), p. 985.

[29] Gao, X., Savic, B., and Baar, R., 2019, "A Numerical Procedure to Model Heat Transfer in Radial Turbines for Automotive Engines," Appl. Therm. Eng., **153**(3), pp. 678–691.
[30] Lim, S. M., Bakhshmand, S. K., Biet, C., and Mihaescu, M., 2020, Experimental and Numerical Investigation of a Turbocharger Turbine Using Exergy Analysis at Non-Adiabatic Conditions. Technical Report, SAE Technical Paper.
[31] Mosca, R., Lim, S., and Mihaescu, M., 2022, "Influence of Pulse Characteristics on Turbocharger Radial Turbine," ASME J. Eng. Gas Turbines Power, **144**(2), p. 021018.
[32] Lim, S. M., 2018, "Aerothermodynamics and Exergy Analysis in Turbocharger Radial Turbine," Ph.D. thesis, KTH Royal Institute of Technology, Stockholm, Sweden.
[33] Moran, M., and Sciubba, E., 1994, "Exergy Analysis: Principles and Practice."
[34] Bejan, A., 2002, "Fundamentals of Exergy Analysis, Entropy Generation Minimization, and the Generation of Flow Architecture," Int. J. Energy Res., **26**(7), pp. 545–565.
[35] Ding, H., Li, Y., Lakzian, E., Wen, C., and Wang, C., 2019, "Entropy Generation and Exergy Destruction in Condensing Steam Flow Through Turbine Blade With Surface Roughness," Energy. Convers. Manage., **196**(3–4), pp. 1089–1104.
[36] Herwig, H., and Kock, F., 2007, "Direct and Indirect Methods of Calculating Entropy Generation Rates in Turbulent Convective Heat Transfer Problems," Heat and Mass Transf., **43**(3), pp. 207–215.
[37] Newton, P., Palenschat, T., Martinez-Botas, R., and Seiler, M., 2015, "Entropy Generation Rate in a Mixed Flow Turbine Passage," International Gas Turbine Congress, Tokyo, Japan, Nov. pp. 15–20.
[38] Bejan, A., 2013, *Entropy Generation Minimization: The Method of Thermodynamic Optimization of Finite-Size Systems and Finite-Time Processes*, CRC press.
[39] Paoletti, S., Rispoli, F., and Sciubba, E., 1989, "Calculation of Exergetic Losses in Compact Heat Exchanger Passages," ASME AES, Vol. 10, pp. 21–29.
[40] Diango, A., Perilhon, C., Descombes, G., and Danho, E., 2011, "Application of Exergy Balances for the Optimization of Non-Adiabatic Small Turbomachines Operation," Energy, **36**(5), pp. 2924–2936.
[41] Hong, B., Venkataraman, V., and Cronhjort, A., 2021, "Numerical Analysis of Engine Exhaust Flow Parameters for Resolving Pre-Turbine Pulsating Flow Enthalpy and Exergy," Energies, **14**(19), p. 6183.
[42] Kazemi Bakhshmand, S., Luu, L. T., and Biet, C., 2021, "Experimental Energy and Exergy Analysis of An Automotive Turbocharger Using a Novel Power-Based Approach," Energies, **14**(20), p. 6572.
[43] Padzillah, M., Rajoo, S., and Martinez-Botas, R., 2014, "Influence of Speed and Frequency Towards the Automotive Turbocharger Turbine Performance Under Pulsating Flow Conditions," Energy Convers. Manage., **80**(5), pp. 416–428.
[44] Yang, M., Martinez-Botas, R., Srithar, R., Ibaraki, S., Yokoyama, T., and Deng, K., 2017, "Unsteady Behaviours of a Volute in Turbocharger Turbine Under Pulsating Conditions."